Ice crystal trajectory simulations in the ICE-MACR compressor rig: fragmentation and melting dynamics

Tristan Soubrié, Jean-Mathieu Senoner, Philippe Villedieu, Martin Neuteboom

▶ **To cite this version:**

Tristan Soubrié, Jean-Mathieu Senoner, Philippe Villedieu, Martin Neuteboom. Ice crystal trajectory simulations in the ICE-MACR compressor rig: fragmentation and melting dynamics. AIAA AVIATION 2022 Forum, Jun 2022, Chicago, United States. pp.AIAA 2022-3535, 10.2514/6.2022-3535 . hal-03740187

HAL Id: hal-03740187
https://hal.science/hal-03740187v1

Submitted on 29 Jul 2022

HAL is a multi-disciplinary open access archive for the deposit and dissemination of scientific research documents, whether they are published or not. The documents may come from teaching and research institutions in France or abroad, or from public or private research centers.

L'archive ouverte pluridisciplinaire **HAL**, est destinée au dépôt et à la diffusion de documents scientifiques de niveau recherche, publiés ou non, émanant des établissements d'enseignement et de recherche français ou étrangers, des laboratoires publics ou privés.

Ice crystal trajectory simulations in the ICE-MACR compressor rig: fragmentation and melting dynamics

Tristan Soubrié*
ANDHEO, Châtillon, 92320, France

Jean-Mathieu Senoner† and Philippe Villedieu‡
ONERA / Université de Toulouse, F-31055 Toulouse, France

Martin O. Neuteboom§
National Research Council of Canada, Ottawa, Ontario, K1A 0R6, Canada

The current work deals with the numerical simulation of ice crystal trajectories within an experimental single stage compressor test rig. First, ice crystal trajectories and the associated fragmentation dynamics within the compressor stage are investigated for different rotor speeds. To this purpose, numerical simulations with two different fragmentation models are compared for cold conditions, i.e. with a sufficiently negative wet bulb temperature to totally inhibit melting. The comparison between the fragmentation models aims at assessing the capabilities of a recently proposed ice crystal fragmentation model with respect to a state of the art model. Both models show good agreement with experimental size distribution data as they reproduce the size reduction of the ice crystals with increasing rotational speed. In a second step, three experimental operating points with wet bulb temperatures raising from negative to positive values and respectively exhibiting no, significant and moderate melting, are simulated. Here, the comparison of numerical and experimental results highlights the strong sensitivity of the ice particles' melt ratio to inlet temperature variations, even by a few degrees.

I. Nomenclature

Dv50	=	Median volumetric diameter
Dvxx	=	Diameter delimiting xx% of the particle volume distribution
ICI	=	Ice crystal icing
OGV	=	Outlet guide vanes
Pstat	=	Static pressure
P0	=	Total pressure
RH	=	Relative humidity compared to vapor saturation, in %
Tstat	=	Static temperature
T0	=	Total temperature
Twb	=	Wet bulb temperature based on static pressure and temperature
Twb0	=	Wet bulb temperature based on total pressure and temperature
TWC	=	Total water content

II. Introduction

Ice crystal icing (ICI) has become a growing safety concern for the aeronautic industry over the last decade. ICI is extremely difficult to tackle through ground-testing and currently not fully addressable with numerical tools. However, being capable of predicting ICI is key from a design, certification, and hence competitiveness point of view, since current

*Director, ANDHEO.
†Research Engineer, DMPE-MH, 2 avenue Edouard Belin, F-31055 Toulouse, France
‡Research Director, DMPE, 2 avenue Edouard Belin, F-31055 Toulouse, France
§Research Officer, National Research Council of Canada.

comparative analysis methods can no longer be used when exploring novel architectures. In particular, aerothermal conditions in the compression system of next generation engines with very high bypass ratios could favor the occurence of ICI.

Icing is normally caused by the freezing of supercooled water droplets upon impact onto solid surfaces. However, an additional risk has been identified over the last decades when flying in clouds with high ice-crystal concentrations (ranging in size from 50 µm to 1 mm) or with mixed phase conditions, i.e. ice crystals combined with supercooled water droplets. Under such conditions, ice accretion may occur on warm parts of the engine compressor, resulting in sudden loss of engine thrust, engine flame-out, and even irreversible damage with permanent power loss. A NASA study published in 2009 [1] identified 140 engine power loss events due to engine core icing since the early 1980's. Newer aircrafts are also affected, as the warnings issued by Boeing in November 2013 regarding their 747-8 and 787 Dreamliner aircrafts, after six incidents in the previous six months, illustrate.

This hazard and its consequences on the engine operability of current as well as future aircraft fleets led to the definition of new certification rules. The Federal Aviation Administration (FAA) proposed new certification requirements for flight in ice-crystal icing conditions (CFR – title 14 – part 33.68 and AC 20-147A). In Europe, work on ICI conditions was also included in the European Aviation Safety (EASA) plan and resulted in the issuing of certification specifications in March 2015 (CS-E Amendment 4 and CS25-Appendix P) which are applicable for all new aircrafts.

For this reason, efforts to improve the predictive capabilities of numerical ICI tools must be pursued to assist in the design of next generation engines and aircrafts. Due to the complexity of current aircraft engine architectures, validation steps of the numerical tools on simplified yet representative configurations appear as a crucial step to reach this objective.

The current work deals with the numerical simulation of ice crystal trajectories within an experimental single stage compressor test rig. First, ice crystal trajectories and the associated fragmentation dynamics within the compressor stage are investigated for different rotor speeds. To this purpose, numerical simulations with two different fragmentation models are compared for cold conditions, i.e. with a sufficiently negative wet bulb temperature to totally inhibit melting. The comparison between the fragmentation models aims at assessing the capabilities of a recently proposed ice crystal fragmentation model with respect to a state of the art model. In a second step, several experimental operating points with wet bulb temperatures raising from negative to positive values and thus exhibiting no, moderate and significant melting, are simulated.

III. ICE-MACR Experiment set-up

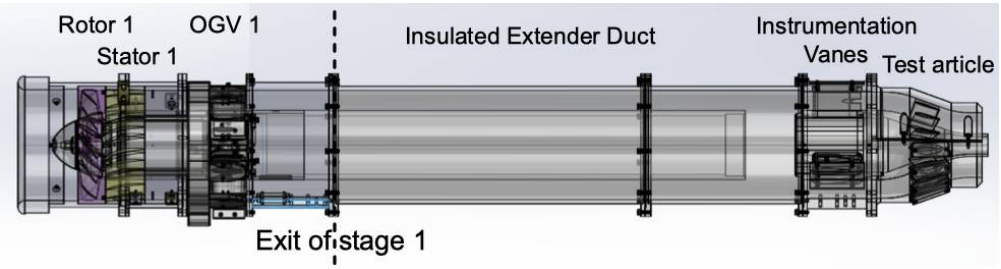

Fig. 1 ICE-MACR module concept in single stage accretion configuration.

ICE-MACR is a modular axial compressor test rig designed by the National Research Council of Canada (NRC). It is dimensioned to operate within icing wind tunnels such as NRC's Altitude Icing Wind Tunnel (AIWT) or Research Altitude Test Facility (RATFac). The purpose of the rig is to simulate ice crystal ingestion into an engine compressor at cruise conditions. The setup considered in the present study is shown in Fig. 1. It consists of a single compressor stage, comprising a rotor, a stator, and an array of uncambered NACA 0018 outlet guide vanes (OGV's). An extender duct is placed downstream the compressor stage in order to enhance ice particle melting. The extender duct is followed by the instrumentation segment to characterize ice crytal properties. It consists of three hollow NACA 0018 struts. The struts contain a rear facing camera to record accretion, the particle detection probe array which measures a radial distribution of particles as well as their passing velocity, a relative humidity probe, a total pressure tap and leading edge thermocouples to measure total temperature. The outer casing of the instrumentation segment holds a pressure tap to measure static pressure. The inner casing of the instrumentation segment includes a radially aligned camera to

observe accretion on the outer casing wall. Finally, a test article consisting of a swan neck duct with guide vanes similar to an inter-compressor duct completes the setup. The test article comprises a 20 degree converging annulus with 15 uncambered NACA 0012 airfoils. The hub and part of the outer shell are semi-transparent. Two borescope cameras pointing radially outwards are installed in the hub, one in line with the airfoil leading edge plane, and one in line with the airfoil trailing edge plane. The overall length of the present ICE-MACR setup is 1.3 m with a casing inner diameter of 145 mm.

IV. Simulation tool

The CFD code CEDRE developed by ONERA [2] is used in the present study. It is a multi-solver platform dedicated to both steady and unsteady flow simulations. In the present computations, two solvers are used: CHARME to simulate the aerodynamic flow field and SPARTE to compute the ice particle trajectories in a Lagrangian framework.

A. Gas solver

The aerodynamic flow solver CHARME solves the Reynolds Averaged Navier-Stokes (RANS) equations for a gas mixture of two species, namely air and water. The $k-\omega$ turbulence model of Menter with SST correction is used [3]. Time integration is performed with an implicit first order Euler scheme associated with a Generalized Minimal RESidual (GMRES) method to solve the linear system. Local time step is used to ensure numerical stability while accelerating convergence. The convective fluxes are calculated with a 2nd order Monotonic Upwind Scheme for Conservation Laws (MUSCL) [4] method and a Harten-Lax-van Leer-Contact (HLLC) scheme [5].

To account for the presence of moving parts in the geometry (rotor), the momentum equations are solved in a rotating frame of reference while maintaining the geometry fixed. Such description yields additional volumetric forces, namely Coriolis and centrifugal forces. The conversion from fixed to rotating frames of reference is then handled via mixing planes. Mixing planes are also used to reduce the computational domain to one blade passage per row and handle the cross section variations from one sector size to another.

Steady computations are performed. Convergence is checked on flow rates, with fluctuations below 0.1%.

B. Lagrangian particle solver

The SPARTE Lagrangian particle solver is used to compute ice-crystal trajectories and exchange phenomena with gas-phase within the test rig.

The Lagrangian dispersed phase approach is based on a direct resolution of the Boltzmann-type equation describing the evolution of the particle density function [6] (spray density function in the nomenclature used in [6]). Its evolution is then computed by approximating the particle density function as a sum of Dirac delta functions centred on each particle sample. This approach allows for a straightforward implementation of physical models and a natural handling of polydispersity. On the contrary, the Lagrangian approach suffers from poor accuracy in regions of low particle density.

First, a few details regarding the underlying numerical algorithms of the ice particle trajectory computation within the test rig are provided. Then the modelling ingredients required to reproduce ice particle trajectories are briefly reviewed. First, the closures necessary to describe the ice crystal motion are presented. Second, phase change, mass and heat exchange phenomena dictating the evolution of particle size, melting and temperature need to be taken into account to predict accretion risks. The interested reader may find further details on most of these aspects in [7]. Finally, particle wall interaction modelling is discussed in detail.

1. Numerical algorithm

The present simulations are steady in the sense that particle trajectories are computed using an averaged flow field for the fluid carrier phase. In addition, two-way coupling effects (e.g. flow field perturbations induced by the particles) are not taken into account. Numerical particles are injected once at the inlet and their trajectories are calculated until they all exit the computational domain, either through the outlet, by entirely sticking on walls or through full evaporation. The evaluation of interphase exchange phenomena between particle and gas require the evaluation of gas properties at the particle position. The latter are reconstructed at the particle's center of gravity using a linear interpolation within the computational cell where the particle is located. The localisation of the particles on the Eulerian grid is performed using an algorithm proposed by Hasselbacher [8].

2. Particle motion

Particle motion is influenced by drag, gravity, added mass and Basset history forces [9, 10]. At high particle to air density ratios (of the order of one thousand) and small particle sizes (less than a few hundred microns), dimensional analysis indicates that drag is largely predominant over all other forces. The expression for particle momentum may thus be written as:

$$m_p \frac{d\vec{u}_p}{dt} = \frac{\pi}{8}\rho_a d_p^2 C_D \left|\vec{u}_a - \vec{u}_p\right| \left(\vec{u}_a - \vec{u}_p\right) \tag{1}$$

An analytical expression for drag is only known for particle Reynolds numbers small compared to unity. However, most practical applications involve finite particle Reynolds numbers so that empirical correlations are required to close the drag term. In addition, ice crystals display shapes that are generally not spherical so that corrections accounting for deviation from sphericity need to be included. In the present case, a correlation proposed by Ganser for isometric particles is used to evaluate the drag coefficient C_D [11]. The latter depends on the particle sphericity ϕ, defined as the ratio of the surface area of a sphere with the same volume as the particle and the projected surface area A of that particle, i.e. $\Phi = \pi d_p^2 / A$.

3. Particle mass and heat transfer phenomena

Three distinct phase-change processes may occur along particle trajectories: sublimation, fusion (melting) and evaporation. These three phase changes are driven by diffusive mass and heat transfer phenomena between the particles and the surrounding gas.

Particle mass transfer is modeled using Spalding's evaporation model [12]:

$$\frac{dm_p}{dt} = -\pi d_p \frac{\mathrm{Sh}}{\Phi}\rho_a D_v \ln\left(1 + B_M\right) \tag{2}$$

with B_M the Spalding mass transfer number:

$$B_M = \frac{y_{v,s} - y_{v,a}}{1 - y_{v,s}} \tag{3}$$

with $y_{v,s}$ and $y_{v,a}$ respectively denote the vapor mass fraction at the particle surface and outside the vapor layer surrounding the particle. Depending on the particle state, which is deduced from its temperature, the mass source term given by the right-hand side of eq. 2 either represents evaporation (partially/fully melted) or sublimation (fully solid).

Heat transfer phenomena at the particle-air interface are driven by heat conduction and the enthalpy variation due to phase change:

$$m_p c_{p,p} \frac{dT_p}{dt} = \pi d_p \frac{\mathrm{Nu}}{\Phi} k_a \frac{\ln\left(1 + B_T\right)}{B_T} \left(T_a - T_p\right) - \dot{m}_p L \tag{4}$$

As for eq. 2, the specific heat capacity at constant pressure $c_{p,p}$ of the particle, the latent heat of phase change L need to be modified according to the particle state, i.e. solid for sublimation, partially/fully melted for evaporation. The Spalding heat transfer number writes:

$$B_T = \left(1 + B_M\right)^{\delta} - 1 \tag{5}$$

with:

$$\delta = \frac{c_{p,v}}{c_{p,g}} \frac{\mathrm{Sh}}{\mathrm{Nu}} \mathrm{Le}_v \tag{6}$$

with $c_{p,v}$, $c_{p,g}$ respectively the heat capacity of the pure vapor species and the gas mixture in the vicinity of the particle, while $\mathrm{Le}_v = \mathrm{Sc}_v / \mathrm{Pr}_v$ represents the Lewis number of the vapor species. The expressions used for Sherwood Sh and Nusselt Nu numbers as well as the modelling for the variation of sphericity Φ are detailed in [13].

4. Wall impingement

The interaction of a (potentially partially melted) ice crystal with a wall is a complex process. The main parameters influencing impact outcomes and dynamics are particle size, impact velocity and degree of metling. In the present work, the two fist parameters are included in the impact model itself while the third parameter is assumed to solely control the deposited masses of solid and liquid.

Two different impact models are compared in the present work. The aim of the comparison lies in the assessment of their respective capabilities in engine like conditions. The first model was proposed by Trontin *et al.* [13] within

the European HAIC project and will be refered to as 'HAIC' model in the following. The second model differs only regarding the description of the fragmentation regime. It was derived within the European MUSIC-haic project in an effort to incorporate basic physical principles between the initial and end states of fragmentation. It will be designated 'MUSIC-haic' model in the following. More details on the MUSIC-haic model may be found in [14].

Both models rely on the same thresholds for the different impact regimes. The classification of impact outcomes is based on the Vidaurre number [15], which represents a ratio of the particle's kinetic energy upon impact (driving fragmentation) with its surface energy (ensuring the particle's cohesion):

$$\mathcal{L} = \frac{\rho_p d_p u_{p,n}^2}{12 e_\sigma} \tag{7}$$

The surface energy of ice is temperature dependent and expressed as

$$e_\sigma(T) = e_{\sigma 0} \exp\left[\frac{Q_s}{R}\left(\frac{1}{T_p} - \frac{1}{T_0}\right)\right]. \tag{8}$$

Vidaurre and Hallett [15] evaluate the initial surface energy as $e_{\sigma 0} = 0.12\,\mathrm{J\,m^{-2}}$ at the reference temperature $T_0 = 253\,\mathrm{K}$.

The classification of impact outcomes established by Trontin *et al.* [13] is used:

$\mathcal{L} < \mathcal{L}_1$	elastic particle bouncing
$\mathcal{L}_1 < \mathcal{L} \leq \mathcal{L}_2$	inelastic particle bouncing
$\mathcal{L} > \mathcal{L}_2$	particle fragmentation

with $\mathcal{L}_1 = 0.5$ and $\mathcal{L}_2 = 90$.

In the two first regimes, the particle diameter remains unchanged: while internal cracks may form in the second regime, the particle is assumed to remain intact. The difference between both regimes then lies in the damping of the incoming normal velocity component ξ. On the contrary, the particle is assumed to shatter in the third regime. The associated size reduction is expected to favor melting and an accurate modelling of fragmentation dynamics is thus important to predict the occurrence of icing.

Regarding the fragments' size characteristics, the HAIC model relates the maximum diameter of the reemited fragments to the Vidaurre number via a power law :

$$d_{p,max} = \left(\frac{\mathcal{L}_2}{\mathcal{L}}\right)^{2/11} d_p \tag{9}$$

Based on the analysis of several experimental databases [14], the MUSIC-haic model derives the size of the largest ice particle fragments within the energy horizon framework proposed by Grady [16]. The latter is based on an energy conservation principle between the initial and end states of fragmentation. The maximum diameter may then be related to the characteristic strain rate $\dot{\varepsilon}$ resulting from impact:

$$\frac{d_{p,max}}{s_0} = C_f \left(\frac{\dot{\varepsilon}}{\dot{\varepsilon_0}}\right)^\alpha \tag{10}$$

with s_0 and $\dot{\varepsilon_0}$ normalization parameters [17] while C_f and α represent the adjustment parameters of the underlying semi-empirical model. Finally, it is assumed that the indentation radius formed upon impact defines the tensile strain levels which eventually cause the particle to shatter. Thus, the strain rate estimate is based on the indentation radius formed upon impact [18, 19] and scales as:

$$\dot{\varepsilon} \sim u_{p,n}^{1/2} d_p^{-1} \rho_p^{-1/4} Y_c^{1/4} \tag{11}$$

with $Y_c = 5.2 \times 10^6$ Pa a reference value for the compressive yield strength of ice. A regression fit to a large experimental dataset then yields $C_f \approx 23.936$ and $\alpha \approx -0.896$. It appears that the improvement regarding the prediction of the maximum fragment diameter with respect to experiments is moderate from the HAIC to the MUSIC-haic model with average error levels being reduced by a few percent with respect to available experimental data [14].

The MUSIC-haic model assumes a power law distribution on the fragment number density function:

$$p_n(d_p) = \frac{\gamma - 1}{d_{p,max}^{\gamma-1} - d_{p,min}^{\gamma-1}} d_p^{-\gamma} \tag{12}$$

with $\gamma = 2.73$ and $d_{p,min} = 0.015 d_{p,max}$, while $d_{p,max}$ is given by eqs. 10 and 11. No reliable experimental data regarding the size distribution of the reemited ice fragments was available when the HAIC model was proposed. It was then arbitrarily assumed that the mass distribution after fragmentation was uniform, corresponding to $\gamma = 3$ in eq. 12. Therefore, the size distributions assumed for both models are coincidentally similar as well. Thus, the main advantage of the MUSIC-haic fragmentation model lies in its reduced degree of empiricism compared to the HAIC model, which could allow for further improvements in ice crystal impact modelling.

The sphericity distribution of the fragments appears difficult to model. In addition, experimental data on this parameter seem very scarce. For this reason, the fragments' sphericity is drawn as a uniform random number within the range $\phi \in [0.6; 1.0]$.

Currently, experiments performed within the MUSIC-haic project only yield access to the radial velocity distribution of the reemited fragments as only the normal velocity of the largest fragment may be measured with the existing experimental set-ups. For this reason, both models share the same correlations for the normal restitution coefficient ξ_{nn} provided by Trontin *et al.* [13], defined as the ratio of the normal velocity components after and before impact. The latter is written as:

$$\xi_{nn} = \begin{cases} 1 & \text{if } \mathcal{L} \leq \mathcal{L}_{c1}, \\ \left(\frac{\mathcal{L}_{c1}}{\mathcal{L}}\right)^{1/3} & \text{if } \mathcal{L} > \mathcal{L}_{c1}. \end{cases} \tag{13}$$

Regarding the damping coefficient of the velocity component tangential to the impinged surface, the latter is assumed equal to unity regardless of the impact velocity, i.e. $\xi_t = 1$.

For the the HAIC model, the restitution coefficient ξ_{nt} describing the tangential velocity component induced by the normal incoming velocity component in case of fragmentation writes:

$$\xi_{nt} = 0.4 \left(1 - \sqrt{\frac{\mathcal{L}_{c2}}{\mathcal{L}}}\right) \tag{14}$$

On the other hand, the MUSIC-haic model interprets this velocity component as resulting from the tensile strain induced upon impact. First, the strain rate given by eq. 11 is interpreted as an average value within the particle. A random distribution of fragments within the original particle given by 12 is then assumed. Finally, the size of a fragment and the location where it forms within the original crystal are assumed decorrelated, i.e. large fragments do not preferentially form towards the center for instance. Expressing eq. 12 in terms of fragment radii r_p instead of diameters for convenience then yields:

$$\begin{aligned} \xi_{nt} &= k \frac{1}{u_{p,n}} \int_{r_{p,min}}^{r_{p,max}} \frac{\gamma - 1}{r_{p,max}^{\gamma-1} - r_{p,min}^{\gamma-1}} r_f^{-\gamma} \int_0^{r_p - r_f} \int_0^{2\pi} \int_0^{\pi} \frac{1}{4/3\pi (r_p - r_f)^3} k\dot{\varepsilon}(r_p + r\cos\theta) r^2 \sin\theta \, dr \, d\theta \, d\phi \, dr_f \\ &= k \frac{3}{32} \pi u_{p,n}^{-1/2} \rho_p^{-1/4} Y_c^{1/4} \left[1 - \frac{1}{r_p} \frac{r_{p,max}^{2-\gamma} - r_{p,min}^{2-\gamma}}{r_{p,max}^{1-\gamma} - r_{p,min}^{1-\gamma}}\right] \end{aligned} \tag{15}$$

The parameter k is then used to adjust the model to the available experimental data, yielding $k \approx 0.909$.

The sticking efficiency ε_{ic}, defined as the ratio of sticking to impinging mass, is assumed to solely depend on particle melt ratio η_m [13]:

$$\varepsilon_{ic} = (K_{ic} - 2)\eta_m^3 + (3 - 2K_{ic})\eta_m^2 + K_{ic}\eta_m \tag{16}$$

with the melt ratio defined as the ratio of particle liquid to total water content.

5. Mixing plane

Similarly to the gas carrier phase, the particle simulations account for the presence of moving parts by resolving the particle equations of motion in a rotating frame of reference and accounting for Coriolis and centrifugal forces. Fix and moving reference frames are also connected via mixing plane boundary conditions. The mixing plane interfaces are split into crowns in the radial direction. Particle properties are mass averaged over each crown and mean values are transferred to the corresponding crown on the other side of the mixing plane. New numerical particles are then injected downstream, with sizes following a log-normal mass distribution that conserves the average upstream diameter and standard deviation. Average melting rate is also conserved per crown, but reinjected particle sizes and melting rates are

imposed so as to conserve correlations that may exist between these parameters. The following centred and normalized random numbers are defined for the melting rate and the particle diameter:

$$x_{d_p} = \frac{d_p - \overline{d_p}}{\sigma_{d_p}} \tag{17}$$

$$x_{\eta_m} = \frac{\eta_m - \overline{\eta_m}}{\sigma_{\eta_m}} \tag{18}$$

where $\bar{\cdot}$ denotes a mass average and $\sigma_{\cdot}$ the associated standard deviation of the considered quantity. The associated correlation matrix may then be defined as:

$$\mathbf{C} = \begin{pmatrix} \rho_{d_p d_p} & \rho_{d_p \eta_m} \\ \rho_{\eta_m d_p} & \rho_{\eta_m \eta_m} \end{pmatrix} \tag{19}$$

with for instance:

$$\rho_{d_p \eta_m} = \overline{x_{d_p} x_{\eta_m}} - \overline{x_{d_p}}\,\overline{x_{\eta_m}} = \overline{x_{d_p} x_{\eta_m}} \tag{20}$$

Thus, the diagonal elements are equal to one given the chosen normalization, i.e. $\rho_{d_p d_p} = \rho_{\eta_m \eta_m} = 1$, and the matrix is symmetric by definition.

First, melting ratio and diameters of the reinjected particles are randomly and independently drawn given their means and variances, yielding x_{d_p} and x_{η_m} according to relations 17 and 18. Then, a correlated vector random vector $\mathbf{x_c}$ may be evaluated from the original random vector $\mathbf{x} = \left[x_{d_p}, x_{\eta_m}\right]$ by a simple matrix vector product

$$\mathbf{x_c} = \mathbf{U}\mathbf{x} \tag{21}$$

with $\mathbf{U}$ the upper triangular matrix of $\mathbf{C}$:

$$\mathbf{C} = \mathbf{U}^{\mathbf{T}}\mathbf{U} \tag{22}$$

which may be obtained via Cholesky decomposition. The procedure outlined above is strictly speaking only valid for random numbers following a normal distribution, which is inaccurate in the present case since both the melting ratio and the particle diameter are positive random variables. Nevertheless, this procedure may still be applied by making the more reasonable assumption that both parameters follow a log-normal distribution, i.e. that the logarithms of their mass averages are normally distributed. The only modifications to be applied are to perform the mass averages on the logarithms of these quantities in eqs. 17, 18, 20 and to take the exponential of the resulting correlated random numbers in the final step. However, this transform does not solve the issue on the unitary upper bound of the melt ratio. For the moment, the variance of the melt ratio is corrected so that the normalized probability mass distribution based on the melt ratio tends to unity when the melt ratio tends to unity. While it was verified that this correction only induced minor changes of the variance in practice, the current procedure clearly requires further improvements. A solution could consist in the use of copulas [20] as they seem to provide a framework allowing to draw random correlated numbers using different probability distributions for each variable.

C. Computation sequence

The two solvers are used in a sequential manner, namely first CHARME, then SPARTE, without feedback impact from a solver to the previous one. Thus, particle momentum, heat and phase exchange phenomena with the gas flowfield are neglected.

V. Mesh

The computational domain is shown on Fig. 2. It consists of five sub-domains, each covering one blade-to-blade passage: rotor, stator, OGV, instrumentation vane, test article, see also with Fig. 1. The 3D CAD of the entire setup as well as the precise locations of all measurement instruments were provided by NRC.

The rotor tip gap is not modeled so that the rotor blade extends up to the shroud. At the rig inlet, the mesh does not extend to the rotation axis but is rather limited to 5 mm in radius.

The mesh has been generated using the AutoGrid™ software. It contains 740,000 heaxahedral cells in total. The first height at the walls is of 0.5 mm, leading to y^+ in the range 5-30. A wall law is applied to determine the wall friction according to the y^+ value.

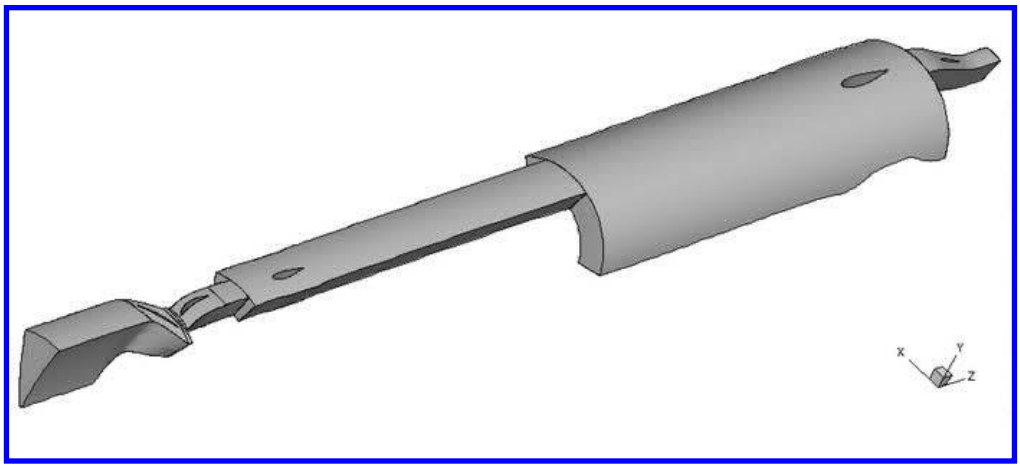

Fig. 2 Computational domain.

Table 1 Rig inlet boundary conditions for the numerical simulations of ice crystal fragmentation without melting, as taken from [22]

Rotor Speed	Pstat	Tunnel speed	Tstat	Nominal centerline TWC
kRPM	kPa	$m\,s^{-1}$	°C	$g\,m^{-3}$
15	34	50	-20	5.0
25	34	50	-20	5.0
33	34	65	-20	6.1

VI. Simulation set-up

A. Test points

First, ice crystal trajectories and the associated fragmentation dynamics within the compressor stage are investigated for different rotor speeds. Cold conditions are considered, i.e. with a sufficiently negative wet bulb temperature to totally inhibit melting. The inlet static temperature is then $-20\,°C$, and the rotor speed ranges from 15 000 to 33 000 RPM, see Table 1. The nominal TWC at $50\,m\,s^{-1}$ is equal to $5.0\,g\,m^{-3}$. It is increased at higher velocities according to the inlet TWC at 50 and $75\,m\,s^{-1}$ provided in [21].

Second, melting of the ice particles travelling through the test rig is investigated considering five operating points with wet bulb temperatures increasing from negative to positive values, thus exhibiting negligible up to significant levels of melting. The points are referred to as Scan #130.02, 132.01, 131.51, 131.31 and 131.01 in the following. Only three of them refer to experimental conditions reported in [21]. In addition, Scan #131.51 and 131.31 define fictitious operating points with conditions lying in-between those of Scans #132.01 and #131.01 and which are used to further characterize the sensitivity of the present numerical simulation to air inlet temperature variations. Rotational speed, pressure and mass flows are constant among all operating points, while the inlet total temperature varies from $-8\,°C$ to $-1\,°C$. The nominal TWC amounts to $3.4\,g\,m^{-3}$.

The three chosen experimental test points result in accretion at various levels of severity. No accretion is observed for Scan #130.02, only limited accretion is observed due to a large average melting ratio of about 40%, corresponding to a severity level of 0.5 following the nomenclature proposed by Neuteboom *et al.* [21]. The most severe accretion was reported for Scan #132.01, with a level of 3.

The operating conditions are summarized in Table 2. Except for the ranges of relative humidity (RH) measured in the tunnel, which were provided by NRC upon direct request, all inout parameters used in the numerical simulations of Scan #130.02, #132.01 and #131.01 correspond to experimental characterizations reported in [21]. Neuteboom *et al.* [21] previously published RH values measured at the test article inlet, but these data are unreliable since they lead to unlikely RH levels over 100% at rig's inlet. Wet bulb temperatures were also reported, but since they strongly depend on RH, they are deliberately omitted in the present paper. Finally, only the air inlet temperature is modified for the two

Table 2 Rig and test article inlet conditions [21] for the numerical simulations involving both fragmentation and melting. In addition to the three experimental operating points, two fictitious operating points (italic) are defined for a sensitivity analysis of the melting process. Only the air inlet temperature is varied for the latter.

	Tunnel	Rig inlet				Rotor	Test article inlet				
	RH	P0	Massflow	T0	TWC	Speed	Melt	Severity	T0 dry	P0	Pstat
Scan #	%	kPa	$kg\,s^{-1}$	°C	$g\,m^{-3}$	RPM	ratio		°C	kPa	kPa
130.02	76-83	34.89	0.308	-8.09	3.4	26290	0.000	0.0	2.04	38.52	36.46
132.01	81-90	34.90	0.300	-3.78	3.4	26300	0.122	3.0	5.41	38.24	36.42
131.51	*92*	*34.90*	*0.300*	*-2.74*	*3.4*	*26300*					
131.31	*93*	*34.90*	*0.300*	*-1.84*	*3.4*	*26300*					
131.01	95-98	34.88	0.300	-0.93	3.4	26300	0.422	0.5	7.51	38.41	36.30

fictitious operating points (Scan #131.51 and 131.31).

B. Boundary conditions

1. Gas

At the rig inlet, total pressure and temperature are specified, either as measured or as calculated from static pressure, temperature and velocity. Dry air is considered to investigate ice crystal fragmentation at low temperature, while humid air is considered to investigate melting. The water vapor fraction is deduced from the maximum RH value measured in the tunnel flow. The RH variations between tunnel and rig inlet due to section restrictions may be considered negligible compared to the variations observed in the tunnel during the experiments.

The massflow rate is set at the outlet, either as measured in the experiments or as calculated from the velocity and thermal conditions at inlet. Radial equilibrium is prescribed at the outlet to correctly reproduce the radial pressure distribution induced by from centrifugal effects.

In the experiment, only the extended duct is insulated. On the contrary, all walls are assumed adiabatic in the numerical simulations. A no slip condition is applied on all walls but the rotor shroud, since the gap at the blade tip is not modelled.

2. Particles

Solid ice crystals are injected at the rig inlet. The experimental particle size distribution measured at 25000 RPM and −20 °C [21] is approximated by a log-normal mass distribution with a mean and standard deviation of respectively 92.2 µm and 0.48. Note that particle mass and volume distribution may be considered equivalent in absence of melting as ice density does not vary significantly with temperature. A comparison between experimental and numerical particle mass size histograms as well as cumulated mass distribution is shown in Figure 3. The same size mass distribution is then used in all computations.

Neuteboom *et al.* [21] reported a non-uniform TWC over the tunnel section. A pronounced peak is observed, aligned with the tunnel centerline and the rig's rotational axis. The outer concentration is only one third of the center value. The SPARTE solver does presently not allow to set a concentration profile depending on the radial position. In an attempt to reproduce the radial concentration profile, the inlet section is subdivided into three crowns with following radial ranges: [5 mm,15 mm], [15 mm,45 mm], [45 mm,72.5 mm]. Figure 4 compares the injected relative TWC profiles with experimental data [21]. The same relative concentration distribution is used in all computations. The nominal inlet TWC, corresponding to the peak value, is adapted for each case.

The sphericity of injected particles is set to $\phi = 0.58$. This parameter was not found to significantly affect results as it only slightly modifies the trajectories up the first impact. This is because the sphericity of the fragments is drawn from a uniform distribution, see section IV.B.4.

Particles are injected with a number density of about $10\,mm^{-2}$. This density must be large enough to ensure satisfactory convergence on the quantities of interest, namely melting ratio and size distributions at various positions within the test rig. It was verified that a multiplication of the injected particle density by a factor 5 had no significant influence on results.

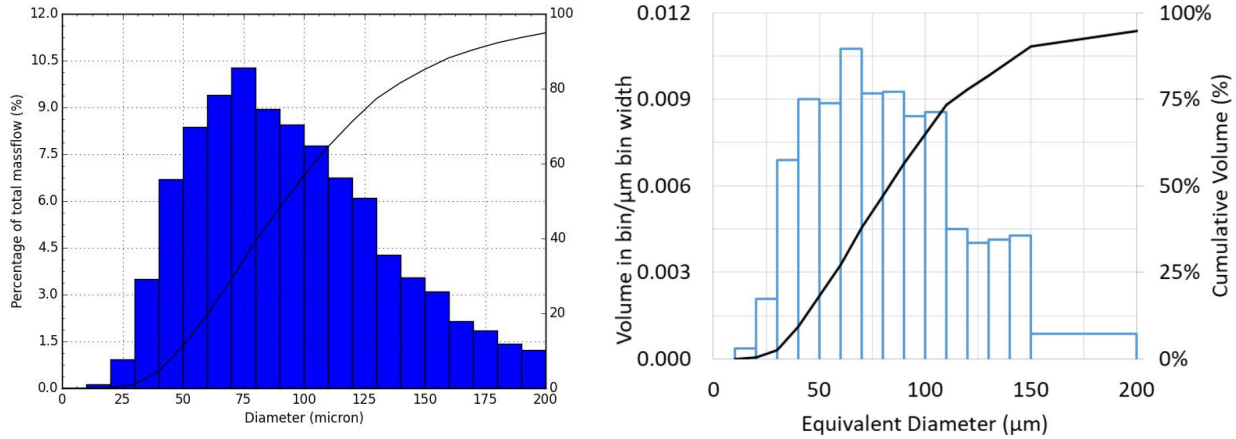

a) b)

Fig. 3 Particle size histograms at inlet to the rig, 25 kRPM, −20 °C**: a) in the computation b) in the experiment [21].**

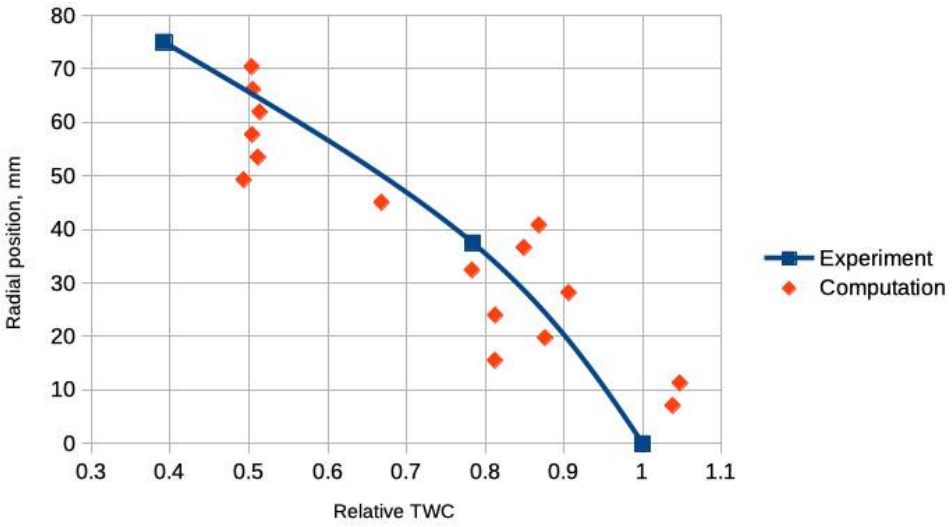

Fig. 4 Rig inlet relative TWC profile, 50 m s^{-1}**,** 25 kRPM**.**

VII. Results for fragmentation

Figure 5 shows the evolution of the particle diameters Dv50 and Dv90 with rotor speed. Here Dvxx corresponds to the diameter delimiting xx% of the fragment volume distribution. Thus, Dv50 corresponds to the median of the fragment volume distribution. Data are extracted at the stage exit. Values plotted at 0 RPM correspond to the size distributions injected at the rig inlet.

Both HAIC and MUSIC-haic impingement models successfully reproduce the decreasing particle size with increasing rotor speed and provide the correct orders of magnitude. The MUSIC-haic model predicts slightly larger sizes than the HAIC model, but the differences between both appear negligible. Both models overestimate the Dv50 at 15 kRPM as well as at 25 kRPM, although to a lesser extent. At 33 kRPM, a very close agreement with experiments is observed for both models. The Dv90 follows a very similar trend as it is also over-estimated at 15 kRPM, slightly under-estimated at 25 kRPM, and correctly captured at 33 kRPM. Overall, the level agreement with experiments appears very satisfactory for both models, especially at 25 kRPM and 33 kRPM.

Figure 6 compares values of Dv10, Dv50 and Dv90 obtained with the MUSIC-haic model at the exit of stage 1 with

values upstream the stator. At 15 kRPM, similar reductions of the Dv50 are observed from the rig inlet to the stator and from the stator to the stage exit. Thus, particle impingement on the spinner / rotor and on the stator/OGV walls almost equally contributes to the size reduction at this rotational speed. On the contrary, most of the ice particle size reduction is caused by impacts on spinner and rotor at higher rotational speeds. The Dv50 reduction between stator and OGV is roughly constant and amounts to approximately 10 µm. Similar trends may be noticed for Dv10 and Dv90.

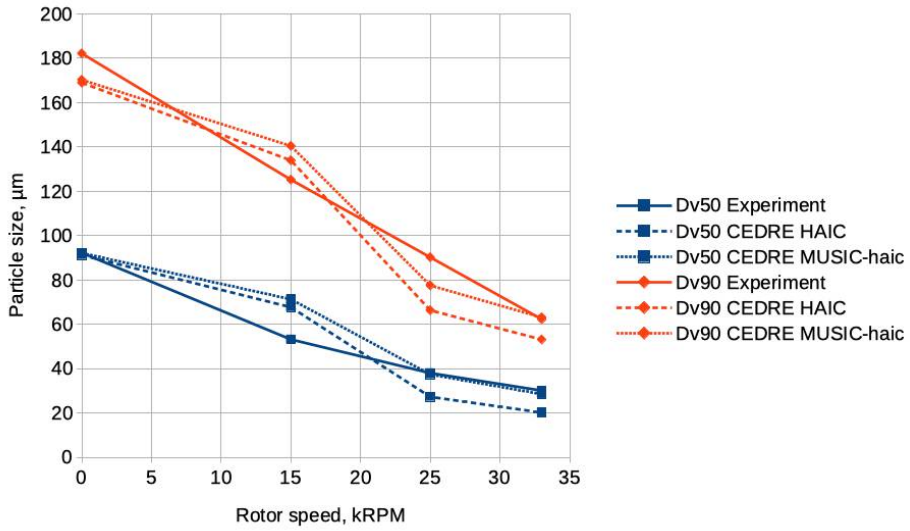

Fig. 5 Particle size with respect to rotor speed, comparison between state-of-art model (HAIC), new model (MUSIC-haic) and experiments at the exit of stage 1.

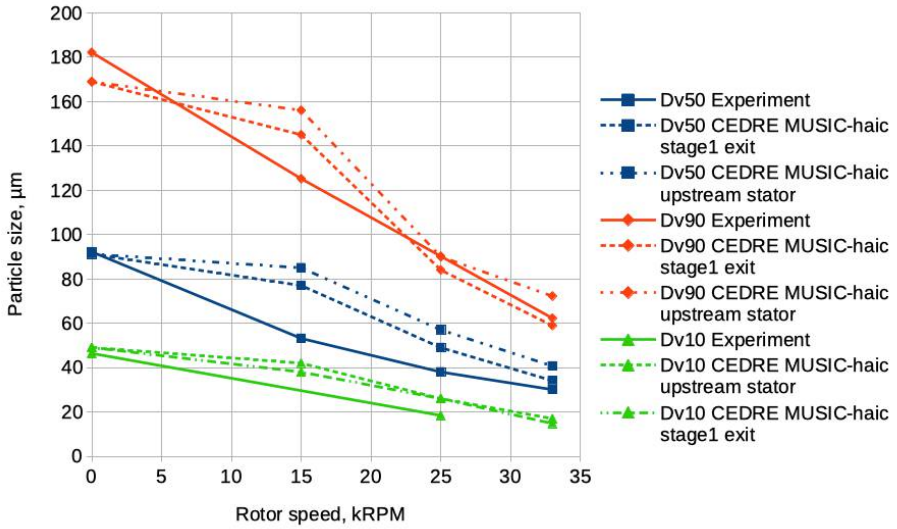

Fig. 6 Particle size with respect to rotor speed. For the numerical simulations, the Dv10, Dv50 and Dv90 obtained downstream the rotor and the exit of stage 1 with the 'MUSIC-haic' model are shown and compared to the experimental values at the exit of stage 1.

The largest impact velocities reported in ice particle experiments are 80 m s^{-1} while the latter reach up to 270 m s^{-1} and 170 m s^{-1} on average at 33 kRPM. Thus, both models seem to correctly extrapolate to impact velocities which are representative of realistic engines. This behavior could be due to the fact that hailstone experimental impact data with significantly larger impact velocities (up to 200 m s^{-1}) were included to callibrate the parameters of these models [14].

The particle size histogram at the exit of stage 1 is plotted for both simulation and experiments on Figure 7. Despite a slight shift towards larger diameters of the numerical volume and cumulated volume distributions compared to experiments, a good agreement may be observed. These results indicate that the numerical averages performed on the mixing plane separating rotor and stator do not significantly deteriorate the size distribution downstream. Note however that a reasonable assumption on the upstream particle size distribution must be made and that its parameters must be computed for each mixing plane crown. As for the rig inlet, the ice crystal particle distributions are assumed to follow a log-normal mass distribution on each mixing plane crown.

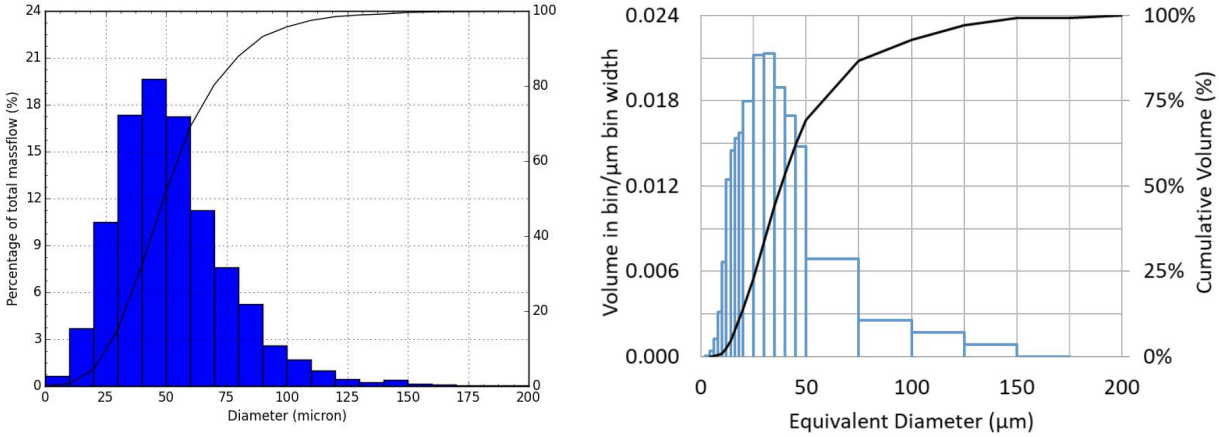

a) b)

Fig. 7 Particle size histograms at stage 1 exit, 25 kRPM, −20 °C**: a) in the computation b) in the experiment [21].**

Figure 8 shows how the radial relative TWC profile evolves with the axial position in the test rig for the case 25 kRPM. To help in the understanding of TWC profiles, particle trajectories are pictured on Fig. 9 in the meridian (z,r) frame. Just upstream the rotor, the relative TWC has increased over 1 at low span due to the rotor spinner. Two peaks are visible at two different radial positions, corresponding to the two angles of the spinner geometry. TWC at low span continues increasing past the rotor, up to 2. At larger radii, the concentration stays similar downstream and upstream the rotor. At the stator exit however, the concentration is drastically reduced over a large portion of the span, and particles concentrate in the upper part. This appears to be due to particle impingement on the spinner and particle centrifugation by the rotor, as illustrated by particle trajectories pictured on Fig. 9 a) or by radial velocities of particles at the interface between rotor and stator (Fig. 10). Impacts on the rotor blade are clearly visible by trajectories pointing out upwards along the trajectories, against the air flow.

The stator casing is not at constant radius but decreases by 3.5 mm over a distance of 94 mm, corresponding to a 2.2° converging conical shape. Most of the particles impinge the casing on this conical portion and bounce off with a negative radial velocity. Thus, trajectories become centripetal due to bouncing, as shown on Fig. 9 b) close to casing, upstream the OGV. The discontinuity in the plot of trajectories corresponds to the mixing plane delimiting the stator/OGV interface on this subfigure. Centrifugal trajectories are still visible upstream the interface, but disappear downstream up to impacts on the OGV blade as shown on Fig. 9 c). This is due to the numerical treatment at the mixing plane: particles are re-injected downstream with the average velocity vector computed from upstream incoming particles. When centripetal and centrifugal trajectories of particles merge, the resulting average velocity is mainly axial. This behavior illustrates the well known issue of crossing trajectories, which occurs when treating a dispersed phase with standard Eulerian methods [23]. While there seems to be no straightforward solution to circumvent this issue, it could be interesting to evaluate its influence on results in future work.

Particles re-injected downstream the stator/OGV mixing plane in annulus' outer portion are isolated on Fig. 9 d). Since they follow centripetal trajectories, they contribute to a spatial redistribution of the particles over the annulus and thus repopulate the inner part of the span. As a consequence, TWC increases in the radius range between [50-65 mm] downstream the OGV compared to the stator exit, as shown on Fig. 8 b) with respect to a). Simulations using the MUSIC-haic model predict three peaks, respectively at 55 mm, 60 mm and 65 mm radii, whereas those using the HAIC

model give a smoother profile around radius 55 mm but similar at larger radial position, although both models give a similar profile downstream the rotor (Fig. 9 a). The predicted level of relative TWC is satisfactory compared to experiment below mid-span, especially with the MUSIC-haic model. No experimental data is currently available at the outermost portion of the annulus. However, it can be deduced from particle mass flow conservation in the system. Conservation applies since the temperature is low enough below 0 °C to limit losses through sublimation or wall deposition. Evaluation of the TWC requires knowledge of the air volumetric flow rate. The latter is evaluated using the radial velocity distribution given by the numerical simulation. The calculated relative TWC close to casing is 2.6 and is plotted on Fig. 8 b) with the explicit mention "extrapolated". Here again, the result compares very well with numerical results.

The radial position of TWC peaks located at radius 60 mm and over is conserved from stage 1 exit to the middle of the extender duct. This probably results from the mostly axial particle injection velocity at the stator/OGV interface. On the contrary, the peak below 60 mm radius is shifted towards the hub, indicating that the centripetal effect induced by particle impacts on the conical casing is still present.

At the inlet of the test article, the relative TWC levels compare again fairly well with experiments as shown on Fig. 8 d). Applying the conservation of water mass flow rate to the experimental profile leads to a relative TWC of 13 at the casing, which is about three times larger than the numerical result. Centrifugal effects within the extender duct could be under-estimated due to the crossing of centrifugal and centripetal velocities at the mixing plane.

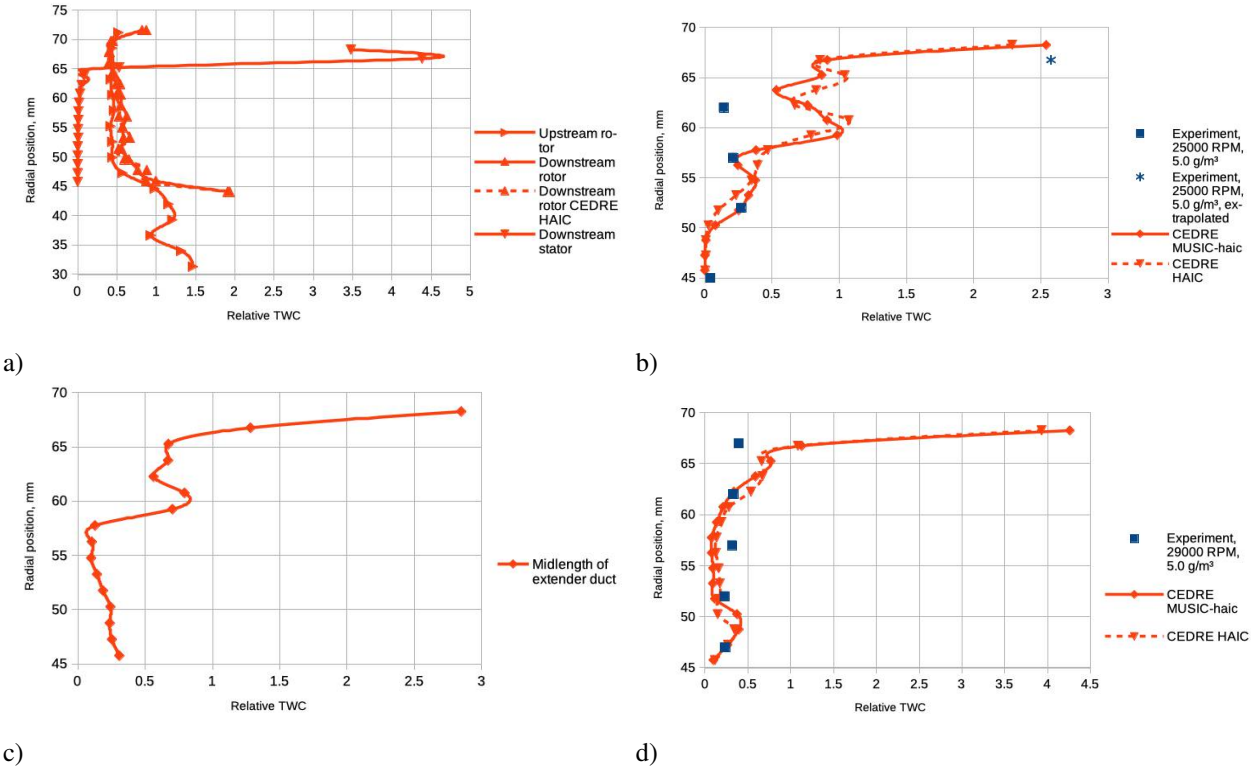

Fig. 8 Radial relative TWC profiles, 25 kRPM**, MUSIC-haic model unless specified: a) in rotor and stator, b) at stage exit, c) at mid-length of the extender duct, d) at inlet to the test article.**

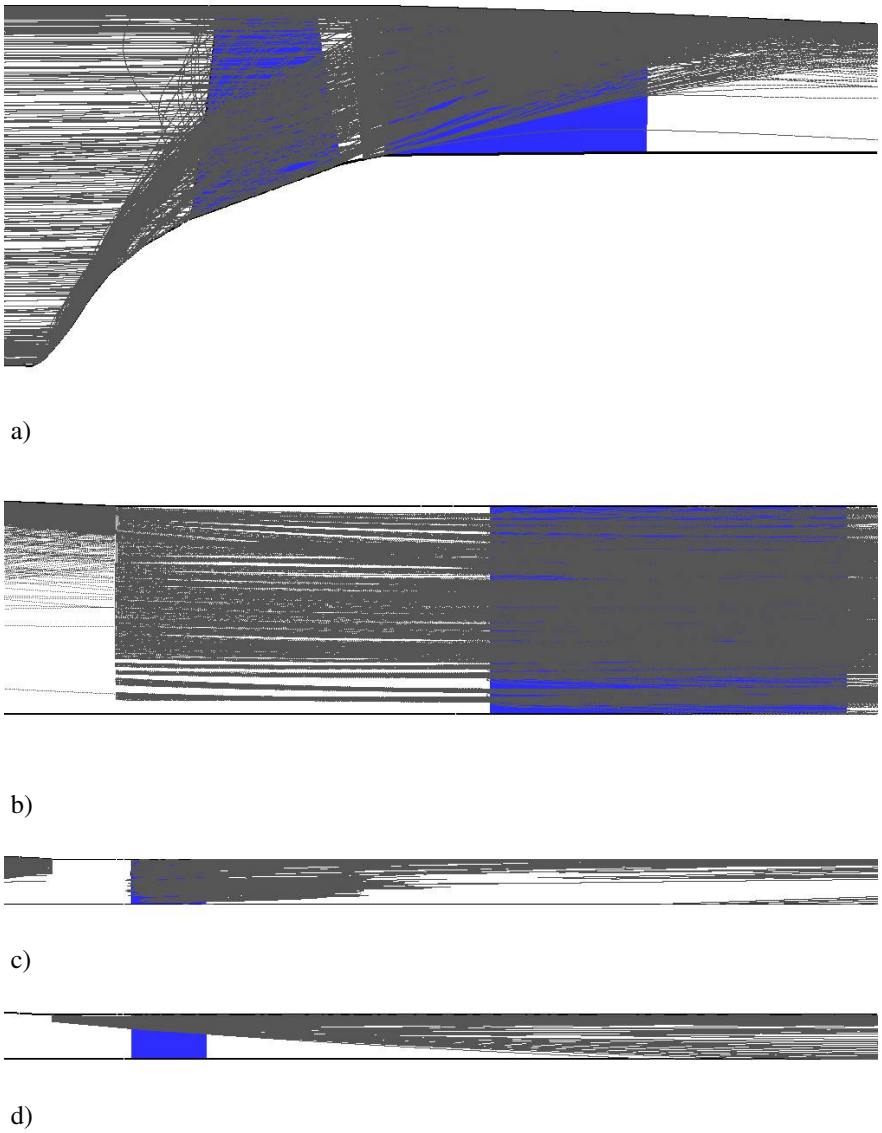

Fig. 9 Trajectories of particles, 25 kRPM**, a) near rotor and stator, b) near OGV, c) limited to centripetal trajectories, d) limited to the outer portion of annulus in the mixing plane.**

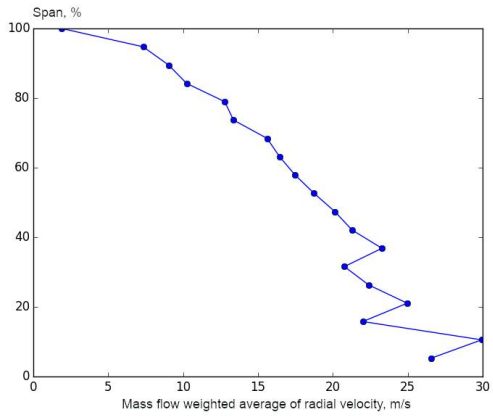

Fig. 10 Radial distribution of particles radial velocity in the plane between rotor and stator, 25 kRPM**.**

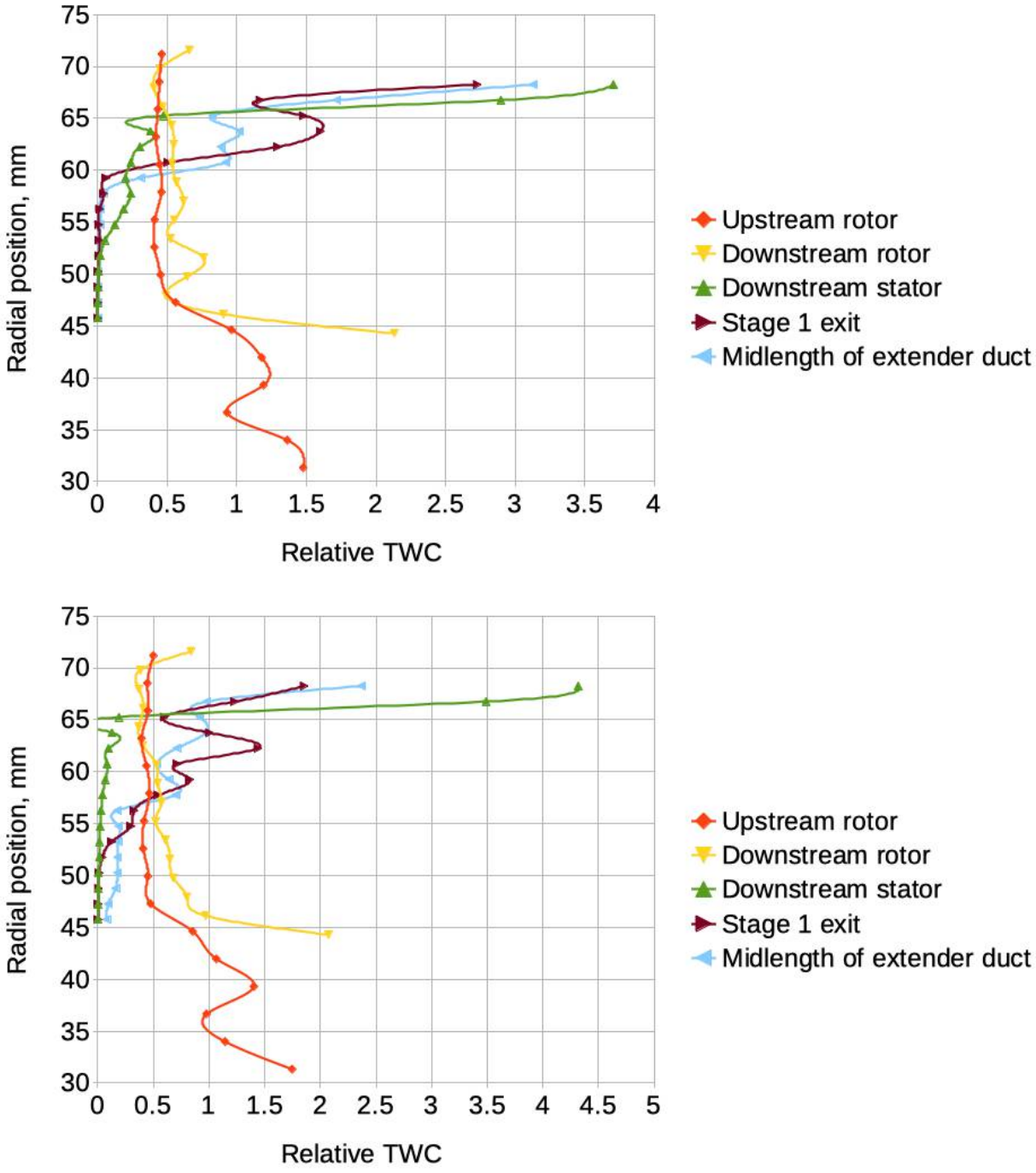

Fig. 11 Radial relative TWC profiles at different locations, 'MUSIC-haic' model, 15 kRPM **(top)** 33 kRPM **(bottom).**

TWC profiles are also plotted for the two other rotor speeds on Fig. 11, while corresponding particle trajectories can be seen on Fig. 12. At lower rotor speed, the effect of centrifugation appears reduced. Then, a large amount of particles impinge on the conical part of the casing. At the stator/OGV interface, centripetal and centrifugal beams are still disjoint. As a consequence, the particles injected on the downstream side of the mixing plane still exhibit centripetal and centrifugal directions according to their radial position, the former being limited to the most outer portion of annulus. The two beams cross just downstream, in front of OGV blade. They are plotted isolated one from each other in the OGV and the extender duct. The increase in TWC at low span is then lower than at 25 kRPM. After bouncing on the casing, particles are redirected towards the hub and merge with the particles following the stator casing slope. The merging of the two trajectory beams produces a peak in the radial range [60-65 mm]. The latter is progressively shifted towards the hub within extender duct.

At 33 kRPM, TWC profile and particle trajectories looks similar to the ones at 25 kRPM.

The average particle velocity measured at instrument vane inlet at 25 kRPM amounts to 82 m s^{-1} in the experiments and 86 m s^{-1} in the numerical simulations.

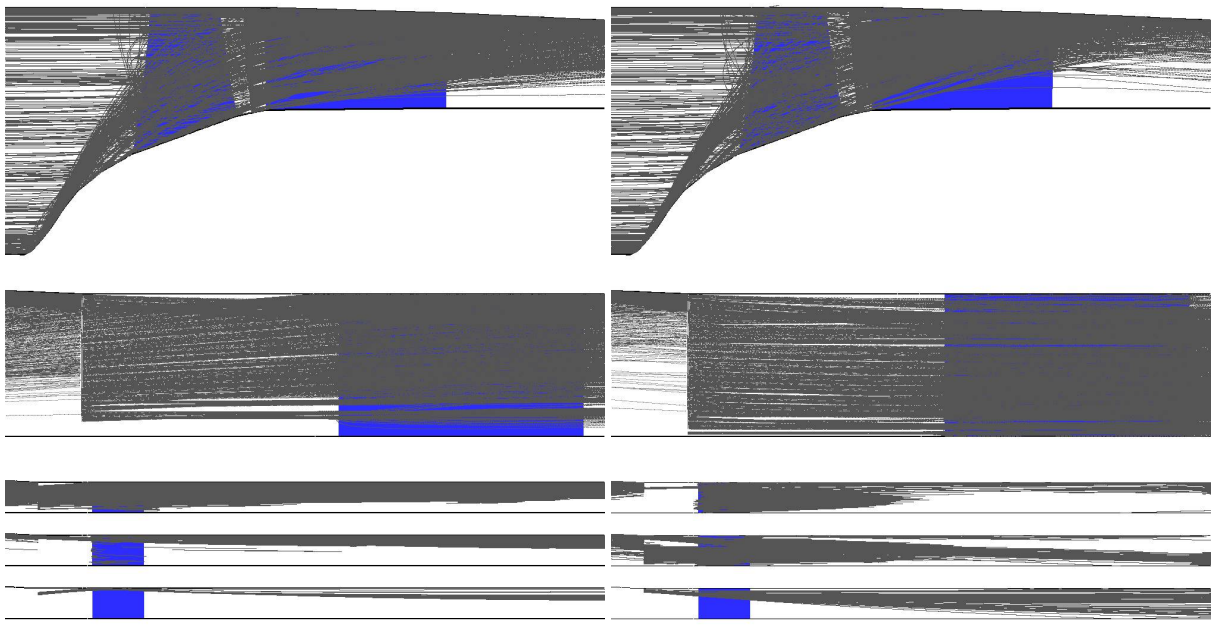

Fig. 12 Trajectories of particles, *left)* 15 kRPM, *right)* 33 kRPM, *top)* near rotor and stator, *middle top)* near OGV, *middle)* limited to centrifugal trajectories, *middle bottom)* limited to centripetal trajectories, *bottom)* some isolated trajectories.

Table 3 Numerical and experimental [21] gas flow parameters in the instrumentation vane.

Scan #	130.02		132.01		131.01	
Parameters	CEDRE	*Experiment*	CEDRE	*Experiment*	CEDRE	*Experiment*
P0, kPa	37.64	*38.52*	37.59	*38.24*	37.55	*38.41*
Pstat, kPa	35.91	*36.46*	35.97	*36.42*	35.87	*36.30*
T0, °C	2.5	*2.04*	6.8	*5.41*	9.7	*7.51*

Table 4 Numerical gas flow parameters at the test article inlet.

Scan #	130.02	132.01	131.51	131.31	131.01
Pstat, kPa	35.92	35.90	35.90	35.89	35.88
Tstat, °C	-0.5	3.8	4.9	5.8	6.7
RH, %	45.7	50.6	52.0	52.8	55.8
Twb, °C	-5.8	-1.7	-0.7	0.2	1.4

Table 5 Melt ratio and temperatures, MUSIC-haic model.

		Melt ratio at test article inlet, %	
Scan #	Inlet T0, °C	CEDRE	*Experiment*
130.02	-8.09	0.0	*0.0*
132.01	-3.78	0.0	*12.2*
131.51	-2.74	0.02	
131.31	-1.84	2.7	
131.01	-0.93	32.7	*42.2*

VIII. Results for melting

A. Gas flow field

To validate the quality of the numerical gas flow field, numerical and experimental data are compared in the instrumentation vane in Table 3. All data are extracted at the experimental probe locations. The total and static pressures are under-estimated by approximately 0.9 kPa and 0.5 kPa, respectively. Either the rotor performance is under-estimated, with a pressure ratio of 1.08 instead of 1.10, or losses in the duct are over-estimated. On the contrary, the total temperature is over-estimated, and the discrepancy increases with the inlet temperature. The difference amounts to 0.5 °C for Scan #130.02, 1.4 °C for Scan #132.01 and 2.2 °C for Scan #131.01. Here again, either the efficiency factor is under-estimated, or thermal losses in the duct are under-estimated. Ongoing discussions with NRC indicate that temperature decreases from 1 to 3 °C were measured between inlet and exit of the extender duct during dry tests, *i.e* in absence of ice particles. Thermal losses may occur at the hub, or by conduction in the insulated casing to upstream and downstream parts. No such effects may be presently captured in the numerical simulations as all walls are assumed adiabatic.

Table 4 provides numerical flow parameters at the inlet to the test article. RH is comprised between approximately 46% and 58%. The Wet bulb temperature increases from largely (−5.8 °C) to slightly (−0.7 °C) negative values. It then reaches positive values of respectively 0.2 °C and 1.4 °C for Scans #131.31 and #131.01. As a consequence, no melting is expected in the numerical simulation of Scan #132.01, contrary to experiments. On the contrary, numerical simulations are expected to predict melting for Scans #131.31 and #131.01.

B. Melting

The ice particles' melt ratio was measured at the inlet to the test article. Table 5 compares measurements and computations performed with the MUSIC-haic impingement model. As expected according to wet bulb temperatures calculated from numerical results, melting is predicted for Scans #131.31 and #131.01, but not for Scan #132.01 contrary to experiments. The amount of melting for scan #131.01 is less than measured but still displays the correct order of magnitude. It is important to remember that melt ratio measurement is not exact but should be considered more as a scale. Indeed, NRC used the ratio of LWC to TWC from the SEA multi-wire probe to get a value. However neither the TWC nor LWC from the SEA multi-wire probe should be considered very accurate. LWC can be as much as 10% low and TWC can be off by a factor of 2-4. LWC also has a false response caused by ice crystals.

The average melt ratio appears to be very sensitive to the inlet temperature. In the experiments, the melt ratio raises from 0 to 12% when increasing the inlet temperature by 4.3 °C, and from 12 to 42% for an additional raise by 2.9 °C. In the simulations, the melt ratio increases from 0.02% to 3% when the inlet temperature raises by 0.9 °C, and a further

temperature raise by 0.9 °C results in a melt ratio of more than 32%. Thus, the numerical simulations appear to predict the onset of melting at larger inlet temperatures compared to experiments. The temperature shift roughly amounts to 2 °C. Moreover, once the onset of melting is reached in the numerical simulations, the latter seem more sensitive to inlet temperature variations compared to experiments. The origin of these discrepancies remains unclear at the moment and will most probably require the evaluation of a variety of error sources.

IX. Conclusion

The present work dealt with the numerical simulation of ice particle fragmentation and melting dynamics within the ICE-MACR single stage compressor test rig. Fragmentation dynamics were investigated for sufficiently cold conditions to totally inhibit melting, allowing to study fragmentation effects separately from melting. Numerical simulations with two different fragmentation models denoted 'HAIC' and 'MUSIC-haic' were examined. It turns out that both models predict very similar fragment size distributions, both for the maximum fragment diameter and the fragment size distribution. Considering particle dynamics after fragmentation, only the predicted radial velocity component differs. Very similar characteristic diameters Dv10, Dv50 and Dv90 were observed for both models at the exit of the single compressor stage. A good agreement with experiments was obtained, especially at higher rotational speeds, i.e. 25 000 RPM and 33 000 RPM. At these higher speeds, most of the fragmentation is induced by particle impingement on the rotor, while impingement on the stator and outlet guide vanes (OGV) significantly contributes to the size reduction at lower rotational speeds (15 000 RPM). Comparison of relative total water contents (TWC) over the radius between numerical simulations and experiments indicate a satisfatory prediction of the ice particles' spatial distribution within the test rig by the numerical simulations. Two distinct trajectory patterns were evidenced: centripetal trajectories for the ice particles impinging on the conical stator casing and centrifugal trajectories for those impinging on the spinner or rotor. It was also observed that these trajectories could cross at mixing plane locations. In such cases, defining the reinjection velocity as the average over all particles crossing a single crown is erroneous and it appears necessary to evaluate the influence of this error on results.

In a second step, different operating points characterized by increasing static inlet air temperatures were simulated. Additional fictitious intermediate operating points were also simulated to further assess melting sensitivity. Discrepancies between simulations and experiments were observed regarding the air flow conditions in the instrumentation vane (where melting is measured in the experiments) and the latter increase with the static air temperature at the inlet. No melting is predicted for most severe accretion experimental operating point (about 12% melt ratio in the experiments) while the correct order of magnitude for melting is captured for the warmest operating point (32.2 % in the numerical simulations vs. 42.2% in the experiments). Thus, the onset of melting is shifted towards higher air inlet temperatures in the numerical simulations. In addition, the latter seem to exhibit higher sensitivity to air inlet temperature variations once melting sets in. The reasons for these discrepancies are currently investigated, it is assumed that uncertainties on relative humidity could play a role, as well as unaccounted temperature losses in the numerical simulations. In addition, the numerical particle volume and cumulated volume distributions appear to be shifted towards larger diameters with respect to experiments at the exit of stage 1 and this effect could also tend to somewhat inhibit melting in the numerical simulations. Finally, the errors on particle trajectories / properties induced by the averaging procedures used at the mixing plane interfaces could also deteriorate numerical results.

Acknowledgments

The funding received within the European Union's Horizon 2020 research and innovation programm under grant agreement No 767560 is gratefully acknowledged.

The authors thank Jennifer Chalmers from NRC of Canada who performed the particle sizing.

T. Soubrié thanks T. Herbez and J. Colomb for their contribution to the computations during their engineer internships.

References

[1] "Technical Compendium From Meetings of the Engine Harmonization Working Group," Tech. Rep. No. DOT/FAA/AR-09/13, FAA, March 2009.

[2] Refloch, A., Courbet, B., Murrone, A., Villedieu, P., C, L., Gilbank, P., Troyes, J., Tessé, L., Chaineray, G., Dargaud, J.-B., Quémerais, E., and Vuillot, F., "CEDRE Software," *Aerospace Lab*, Vol. 2, 2011.

[3] Menter, F. R., "Improved two-equation k-omega turbulence models for aerodynamic flows," *Nasa Sti/recon Technical Report N*, Vol. 93, 1992, p. 22809.

[4] Osher, S., "Convergence of generalized MUSCL schemes," *SIAM Journal on Numerical Analysis*, Vol. 22, No. 5, 1985, pp. 947–961.

[5] Harten, A., Lax, P. D., and Leer, B. v., "On upstream differencing and Godunov-type schemes for hyperbolic conservation laws," *SIAM review*, Vol. 25, No. 1, 1983, pp. 35–61.

[6] Williams, F. A., "Spray combustion and atomization," *The physics of fluids*, Vol. 1, No. 6, 1958, pp. 541–545.

[7] Norde, E., Senoner, J.-M., van der Weide, E. T. A., Trontin, P., Hoeijmakers, H. W. M., and Villedieu, P., "Eulerian and Lagrangian ice-crystal trajectory simulations in a generic turbofan compressor," *Journal of Propulsion and Power*, Vol. 35, No. 1, 2019, pp. 26–40.

[8] Haselbacher, A., Najjar, F. M., and Ferry, J. P., "An efficient and robust particle-localization algorithm for unstructured grids," *Journal of Computational Physics*, Vol. 225, No. 2, 2007, pp. 2198–2213.

[9] Maxey, M. R., and Riley, J. J., "Equation of motion for a small rigid sphere in a nonuniform flow," *The Physics of Fluids*, Vol. 26, No. 4, 1983, pp. 883–889.

[10] Gatingol, R., "The Faxen formulae for a rigid particle in an unsteady non-uniform Stokes flow," *Journal de Mécanique Théorique et Appliquée*, Vol. 1, No. 2, 1983, pp. 143–160.

[11] Ganser, G. H., "A rational approach to drag prediction of spherical and nonspherical particles," *Powder technology*, Vol. 77, No. 2, 1993, pp. 143–152.

[12] Sirignano, W. A., and Edwards, C. F., "Fluid dynamics and transport of droplets and sprays," *Journal of Fluids Engineering*, Vol. 122, No. 1, 2000, pp. 189–190.

[13] Trontin, P., Blanchard, G., and Villedieu, P., "A comprehensive numerical model for mixed-phase and glaciated icing conditions," *8th AIAA Atmospheric and Space Environments Conference*, 2016, p. 3742.

[14] Senoner, J. M., Trontin, P., Reitter, L., Karpen, N., Schremb, M., Vargas, M., and Villedieu, P., "Ice particle impact on solid walls: size modeling of reemited fragments," *Submitted to International Journal of Impact Engineering*, 2021. Preprint available at `https://www.researchgate.net/publication/357556988_Ice_particle_impact_on_solid_walls_size_modeling_of_reemited_fragments`.

[15] Vidaurre, G., and Hallett, J., "Particle Impact and Breakup in Aircraft Measurement," *Journal of Atmospheric and Oceanic Technology*, Vol. 26, No. 5, 2015, pp. 972–983.

[16] Grady, D., "The spall strength of condensed matter," *Journal of the Mechanics and Physics of Solids*, Vol. 36, No. 3, 1988, pp. 353–384.

[17] Glenn, L., and Chudnovsky, A., "Strain-energy effects on dynamic fragmentation," *Journal of Applied Physics*, Vol. 59, No. 4, 1986, pp. 1379–1380.

[18] Hutchings, I., "Strain rate effects in microparticle impact," *Journal of Applied Physics*, Vol. 10, No. 14, 1977, p. L179.

[19] Roisman, I., and Tropea, C., "Impact of a crushing ice particle onto a dry solid wall," *Proceedings of the Royal Society A: Mathematical, Physical and Engineering Sciences*, Vol. 471, No. 2183, 2015, p. 20150525.

[20] Nelsen, R. B., *An introduction to copulas*, Springer Science & Business Media, 2007.

[21] Neuteboom, M. O., Chalmers, J. L. Y., , and Davison, C. R., "Ice Crystal Environment - Modular Axial Compressor Rig: Overview of Altitude Icing Commissioning," *2020 AIAA Aviation Forum*, 2020, p. 2823.

[22] Chalmers, J. L. Y., Wiebe, M., Neuteboom, M. O., and Davison, C. R., "Ice Crystal Environment Modular Axial Compressor Rig: Characterization of Particle Fracture and Melt Across One Rotor Using Laser Shadowgraph," *2020 AIAA Aviation Forum*, 2020, p. 2825.

[23] Desjardins, O., Fox, R. O., and Villedieu, P., "A quadrature-based moment method for dilute fluid-particle flows," *Journal of Computational Physics*, Vol. 227, No. 4, 2008, pp. 2514–2539.